

Electric Field Model of Transcranial Electric Stimulation in Nonhuman Primates: Correspondence to Individual Motor Threshold

Won Hee Lee, *Member, IEEE*, Sarah H. Lisanby, Andrew F. Laine, *Fellow, IEEE*,
and Angel V. Peterchev*, *Member, IEEE*

Abstract—Objective: To develop a pipeline for realistic head models of nonhuman primates (NHPs) for simulations of noninvasive brain stimulation, and use these models together with empirical threshold measurements to demonstrate that the models capture individual anatomical variability. **Methods:** Based on structural MRI data, we created models of the electric field (E-field) induced by right unilateral (RUL) electroconvulsive therapy (ECT) in four rhesus macaques. Individual motor threshold (MT) was measured with transcranial electric stimulation (TES) administered through the RUL electrodes in the same subjects. **Results:** The interindividual anatomical differences resulted in 57% variation in median E-field strength in the brain at fixed stimulus current amplitude. Individualization of the stimulus current by MT reduced the E-field variation in the target motor area by 27%. There was significant correlation between the measured MT and the ratio of simulated electrode current and E-field strength ($r^2 = 0.95$, $p = 0.026$). Exploratory analysis revealed significant correlations of this ratio with anatomical parameters including of the superior electrode-to-cortex distance, vertex-to-cortex distance, and brain volume ($r^2 > 0.96$, $p < 0.02$). The neural activation threshold was estimated to be 0.45 ± 0.07 V/cm for 0.2-ms stimulus pulse width. **Conclusion:** These results suggest that our individual-specific NHP E-field models appropriately capture individual anatomical variability relevant to the dosing of TES/ECT. These findings are exploratory due to the small number of subjects. **Significance:** This study can contribute insight in NHP studies of ECT and other brain stimulation interventions, help link the results to clinical studies, and ultimately lead to more rational brain stimulation dosing paradigms.

Index Terms—Electric field model, electroconvulsive therapy, finite element method, magnetic resonance imaging, motor threshold, nonhuman primate, transcranial electric stimulation.

I. INTRODUCTION

DUE to physiological and behavioral similarities between humans and nonhuman primates (NHPs), NHP studies

Manuscript received November 8, 2014; revised January 22, 2015 and April 19, 2015; accepted April 20, 2015. Date of publication April 22, 2015; date of current version August 18, 2015. This work was supported by the National Institutes of Health under Grant R01MH091083. *Asterisk indicates corresponding author.*

*A. V. Peterchev is with the Departments of Psychiatry and Behavioral Sciences, Biomedical Engineering, and Electrical and Computer Engineering, Duke University, Durham, NC 27710 USA (e-mail: angel.peterchev@duke.edu).

W. H. Lee is with the Icahn School of Medicine at Mount Sinai.

S. H. Lisanby is with the Duke University.

A. F. Laine is with the Columbia University.

Color versions of one or more of the figures in this paper are available online at <http://ieeexplore.ieee.org>.

Digital Object Identifier 10.1109/TBME.2015.2425406

are increasingly deployed to develop mechanistic understanding and to optimize noninvasive brain stimulation as a research and therapeutic tool. Studies in NHPs, especially rhesus macaques, have explored noninvasive brain stimulation techniques such as electroconvulsive therapy [ECT—a form of transcranial electric stimulation (TES)] [1]–[5], transcranial magnetic stimulation (TMS) [6]–[10], and focused ultrasound [11].

To characterize the effect of transcranial electric and magnetic stimulation on the brain as well as to optimize and individualize dosing paradigms, computational models of the electric field (E-field) induced in the brain, typically based on structural magnetic resonance imaging (MRI) data, are increasingly used in human studies [12]–[14]. Such models have not been developed for NHPs, however. For generating an anatomically-accurate NHP model, one critical requirement is tissue segmentation of the head to represent the complex tissue geometries. While there are a plethora of available segmentation tools to extract different tissue compartments from the human MRI images, they are developed and fine-tuned for the human brain MRI data and not for NHPs which have smaller brain sizes and different brain anatomy.

Addressing this need, in this paper we present a pipeline for creating finite element (FE) models of rhesus macaques—the NHP most commonly used in research. Specifically, we develop realistic volume conductor models of four NHP heads incorporating tissue heterogeneity and tissue conductivity anisotropy. To demonstrate their utility, we use the head models and the finite element method (FEM) to compute the spatial distribution of the E-field strength generated by the right unilateral (RUL) ECT electrode configuration. Leveraging the individual models, we investigate the effect of anatomical differences on the E-field strength in the brain across the four subjects at fixed stimulus current amplitude to assess whether current individualization is needed. Our previous work with simplified spherical models suggested that stimulus current individualization in ECT may be appropriate to compensate for individual anatomical differences [15], [16]. Reduced and individualized current amplitude of ECT could potentially reduce its adverse cognitive side effects [16], [17].

Furthermore, to demonstrate the models' capability to inform stimulation dose selection, we combine the models of the four NHPs with *in vivo* measurements of their motor threshold (MT) with TES. The MT, defined as the lowest stimulus pulse amplitude required to elicit a muscle twitch, is commonly used in TMS to individualize the amplitude of stimulus trains [18], [19],

since it captures the effect of anatomical variability on the E-field induced in the brain as well as individual variation in neural excitability [20]. We have proposed that MT determined by administering TES through the ECT electrodes could be used to individualize the current amplitude in ECT [3]. We test whether individual differences in TES MT can be predicted by individual anatomical variability as captured by the subject-specific E-field simulation models. We also explore some macroscopic anatomical characteristics of the head that drive the individual differences in the induced E-field strength.

Finally, we use the combination of realistic individual E-field models and corresponding empirical MT data to estimate the threshold E-field magnitude needed for neural activation with TES/ECT. Previous estimates of the neural activation threshold in ECT studies were mostly based on TMS which has different pulse shape and E-field focality characteristics [21]. Therefore, a neural activation threshold determined with TES using ECT pulse shape and electrode configuration could be more relevant to ECT studies.

Preliminary results from this study were previously presented in part in conference proceedings [22].

II. MATERIALS AND METHODS

The steps of the E-field modeling and analysis are diagrammed in Fig. 1 and described below.

A. Structural and Diffusion Tensor MRI Acquisition

All studies were approved by the Institutional Animal Care and Use Committees of New York State Psychiatric Institute, Columbia University, and Duke University. T1-weighted MRI and diffusion-weighted imaging (DWI) datasets of four healthy male rhesus macaques (*Macaca mulatta*) (age = 12–18 years; weight = 8.4–10.7 kg) were acquired on a Siemens 3 T Trio scanner (Siemens, Erlangen, Germany) using an eight-channel knee coil. The NHPs were sedated with a combination of ketamine HCl (3 mg/kg body wt. IM) and dexdomitor (0.075 to 0.15 mg/kg body wt. IM) and transported to the MRI unit in approved transport cages. Prior to MRI scanning, the NHPs were intubated with a 4 to 5 mm tube for administration of isoflurane gas anesthesia (0.5% to 3%). The NHPs were oriented in a sphinx position with the head forward and were continuously monitored by an Invivo (Essential) MRI-compatible patient monitor. Vital signs monitored included heart rate and blood oxygenation (SpO₂). The T1-weighted MRI images were acquired with a 3-D magnetization prepared rapid gradient echo (MPRAGE) sequence (TR = 2300 ms; TE = 4.4 ms; TI = 1100 ms; 256 coronal slices; $0.7 \times 0.7 \times 0.7$ mm³ voxel; FA = 8°; two averages). The DWI data were acquired by employing a single-shot spin-echo echo-planar imaging (EPI) sequence (TR = 13000 ms; TE = 81 ms; 128×128 matrix; $1.4 \times 1.4 \times 1.4$ mm³ voxel; interleaved acquisition; pixel bandwidth = 1346 Hz). The diffusion sensitizing gradients with a *b*-value of 1000 s/mm² were applied in 12 noncollinear directions. Six image volumes with nondiffusion weighting (*b* = 0 s/mm²) were also acquired as reference images. A twice-refocused technique was used to minimize eddy current effects induced by

strong diffusion-weighting gradients [23]. The generalized autocalibrating partially parallel acquisitions (GRAPPA) parallel imaging scheme with an acceleration factor of two was applied to reduce susceptibility artifacts and to improve the SNR [24]. A partial Fourier algorithm of a factor of 0.75 was used to reduce the EPI echo train length, which further ameliorated geometric distortion [25]. DWI acquisition was repeated six times and averaged to increase the SNR.

B. Preprocessing and Tissue Segmentation

We extracted the NHP head regions from background noise and artifacts using a morphological processing technique including thresholding, opening, and closing of the head binary masks [26]. The preprocessing of the extracted head MR volume was performed based on the open source software components available within 3-D Slicer 4.0 [27] and in-house image processing algorithm [26]. The head MRI images were upsampled ($0.5 \times 0.5 \times 0.5$ mm³ voxel), and were spatially oriented along manually-defined anatomical landmarks, corresponding to anterior commissure (AC), posterior commissure (PC), and fiducials for interhemispheric midline, so that AC–PC line was perpendicular to the coronal plane, and the midline plane was aligned with the sagittal plane. The AC–PC alignment process provides a common orientation for each brain while maintaining the original size of the brain intact. The MRI image intensities were corrected for bias field inhomogeneities that otherwise would reduce the accuracy of tissue segmentation [28]. We then applied content-preserving anisotropic diffusion filtering to remove the image noise while preserving content details and enhancing tissue boundaries [29]–[31]. Finally, nonbrain regions were removed using the skull-stripping algorithm BET tool in FSL 4.1 (FMRIB Analysis Group, University of Oxford, U.K.) [32]. This initial segmentation was further corrected for accurate brain volume extraction using manual editing tools in ITK-SNAP software [33].

We implemented an automatic algorithm that uses the unified segmentation routines [34] implemented in SPM8 (Wellcome Department of Cognitive Neurology, Institute of Neurology, University College London, U.K.) to produce probability tissue maps that define the probability of occurrences of a given tissue for each voxel of the image. Among various available segmentation tools (see discussion in [35]), we selected SPM8 since its unified segmentation approach is fully automatic [34]. Furthermore, it was successfully tested with the macaque tissue priors [36] and performed better than other available tools for the NHP brain segmentation [37].

The deskulled NHP MRI images were segmented into tissue probability images in native space corresponding to gray matter, white matter, and cerebrospinal fluid (CSF) based on the 112RM-SL macaque tissue priors [36]. In this process, the unified segmentation approach uses an objective cost function integrating the prior tissue probabilities, a mixture of Gaussians, and a registration term [34]. Instead of the default settings in the “Segment” tool in SPM8, our algorithm utilized user-defined parameter settings: 1) human tissue priors (ICBM452 T1-weighted average) were replaced by the 112RM-SL macaque tissue priors

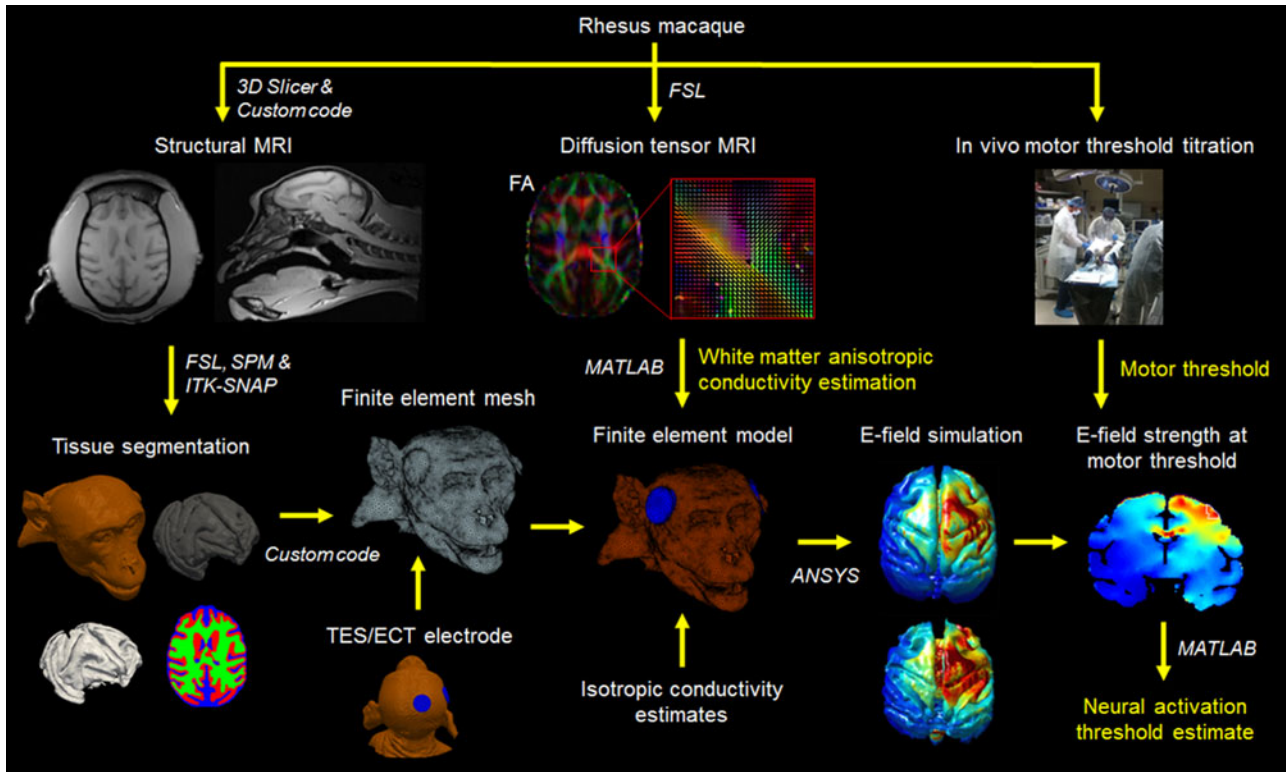


Fig. 1. Overview of the workflow for generating a realistic FE model of TES in NHPs for E-field computation and combining it with *in vivo* MT data to estimate neural activation threshold. T1-weighted MRI and diffusion tensor MRI data sets of the NHP subjects are acquired. The T1-weighted MRI data are preprocessed using 3-D slicer and in-house image processing pipelines. The T1-weighted MRI images are segmented into 14 tissues using FSL, SPM and ITK-SNAP: Example segmentation of the rhesus macaque head shows 3-D surface renderings of skin (brown), gray matter (dark gray), and white matter (light gray), and 2-D masks of cerebrospinal fluid (CSF, blue), gray matter (red), and white matter (green). The color-coded fractional anisotropy (FA) map and diffusion tensor ellipsoids (enlarged view of the region framed in red) represent the principal orientations (largest eigenvectors) of the tensors (red: left–right, green: anterior–posterior, and blue: superior–inferior). Diffusion tensor data are processed and registered to structural MRI data using FSL. White matter anisotropic conductivity tensors are estimated within MATLAB. RUL TES electrodes are incorporated into the head model. The complete 3-D TES models are discretized into FE meshes, and the FE models are completed by assigning the tissue electrical conductivities. The E-field distribution is computed using the FE method with ANSYS. MT is titrated *in vivo* by the current amplitude of single stimulus pulses. Neural activation threshold is estimated by extracting the simulated E-field strength in the target motor area at the empirical MT current. The E-field strength induced in the brain by the RUL TES electrode configuration is computed at the empirical MT current.

[36]; 2) affine regularization was changed to “average sized template;” 3) sampling distance was reduced to 2 mm [37]. Manual segmentation of the nonbrain regions into 11 tissue compartments, representing skin, muscle, skull spongiosa, skull compacta, vertebrae, spinal cord, lens, eyeball, sclera, optic nerve, and sinus, was carried out using a combination of segmentation editing tools from the ITK-SNAP software [33] and an in-house morphological segmentation algorithm [26], [29].

C. TES FE Model Generation

We modeled the RUL electrode placement which is standard in clinical ECT [38]. The electrodes are round with a diameter of 2.5 cm (half of the diameter of human electrodes due to the smaller size of the NHP head). One electrode was centered 1.25 cm to the right of vertex and the second electrode was placed in the homologous right frontotemporal position (see Fig. 1). The contact surface between each electrode and the skin was defined by the outer surface of the NHP head. Subsequently, we applied an adaptive FE meshing technique to the individual NHP head models incorporating the stimulation electrodes, see details [26]. The four individual-specific TES FE models of the

rhesus macaque heads and electrodes were created by means of the restricted Delaunay tessellation algorithm [39], [40], each consisting of approximately 1.8 million tetrahedral elements.

D. Tissue Conductivity Assignment

We created volume conductor head models by assigning anisotropic electrical conductivities to the white matter compartment, and isotropic conductivities to all other tissue regions. The isotropic electrical conductivities (in S/m) are given in Table I [26], [41]–[46].

The estimation of the anisotropic conductivity tensors in the white matter started with preprocessing of the raw DWI head data. The NHP DWI data were processed using FSL’s diffusion toolbox from the FMRIB Software Library. Artifacts and spatial distortions due to eddy current effects caused by strong diffusion gradients used in the EPI sequence and possible head motion were corrected by performing an affine registration between diffusion-weighted images and nondiffusion-weighted images. For each of the four NHP DWI datasets, the diffusion-weighted volumes were coregistered to the nondiffusion-weighted volume, which was used as the reference volume. A binary brain

TABLE I
TISSUE ELECTRICAL CONDUCTIVITIES (S/M)

Tissue	Conductivity	Tissue	Conductivity
Skin	0.43	Lens	0.32
Muscle	0.32	Eyeball	0.5
Skull compacta	0.0063	Sclera	0.5
Skull spongiosa	0.04	Spinal cord	0.15
CSF	1.79	Vertebrae	0.012
Gray matter	0.33	Optic nerve	0.14
White matter (iso.)	0.14	Sinus	0

mask was extracted from the volume with nondiffusion weighting in diffusion space using FSL's BET tool. The segmentation errors resulting from the automated segmentation algorithm were further corrected to ensure that we only reconstructed diffusion tensors inside the brain rather than the surrounding air. We then computed the diffusion tensors for each voxel of the preprocessed DWI datasets [47]. The resulting diffusion tensor volumes were coregistered to the structural T1-weighted MRI volume using an affine registration with mutual information as the cost function while the orientation of each diffusion tensor was preserved [48]. The electrical conductivity tensors σ in the white matter were computed from the measured diffusion tensors D and the isotropic white matter conductivity σ_{iso} from the literature using the "volume normalized" approach [49]–[54]: In each voxel, the diffusion tensor is linearly scaled so that the volume of the resulting conductivity tensor ellipsoid matches that of an isotropic conductivity tensor sphere with radius σ_{iso}

$$\sigma = \frac{\sigma_{\text{iso}}}{\sqrt[3]{d_1 \cdot d_2 \cdot d_3}} D \quad (1)$$

where d_i are the diffusion tensor eigenvalues. This approach preserves the orientation (eigenvectors) and anisotropy ratios (eigenvalue ratios) of the diffusion tensors.

E. Electric Field Computation

Each of the realistic TES FE models along with the electrical conductivity values was imported into the FE analysis software ANSYS (ANSYS, Inc., Canonsburg, PA). Due to the low frequency content (< 10 kHz) of the stimulus current of conventional TES and ECT devices, the quasi-static approximation can be deployed to simplify the E-field simulation by neglecting wave propagation, capacitive, and inductive effects [39], [55]. Thus, the E-field solutions were obtained by solving the Laplace equation with no internal sources [26]

$$\nabla \cdot (\sigma \nabla V) = 0 \quad (2)$$

where V and σ denote the electric potential and tissue electrical conductivity tensor, respectively. The linear equation system of the FEM was solved using the preconditioned conjugate gradient solver (relative tolerance = 1×10^{-8}) within ANSYS. The E-field distribution was determined by taking the gradient of the scalar potential V .

F. In Vivo MT Titration

We determined the MT corresponding to the amplitude of a single TES pulse required to elicit a motor response in sedated NHPs [3]. The NHP subjects were sedated with ketamine (5–10 mg/kg i.m.) and xylazine (0.35–0.7 mg/kg i.m.) [1]. The electrode sites were prepared by cleaning with alcohol to remove scalp oils and then rubbing with an abrasive gel (NuPrep, Weaver and Co., Aurora, CO) to reduce impedance. Thymapad adhesive electrodes (Somatics, LLC, Lake Bluff, IL) were cut down to 2.5 cm circles. The MT was titrated by stepping the amplitude of single stimulus pulses (pulse width = 0.2 ms) delivered through the RUL ECT electrodes with a DS7AH high-voltage constant-current stimulator (Digitimer, Welwyn Garden City, Hertfordshire, U.K.). Electromyography was measured with needle electrodes from the first dorsal interosseous (FDI) muscle in the left hand, since the RUL electrode configuration predominantly stimulates the right hemisphere [26]. We determined the MT as the lowest stimulus pulse amplitude needed to achieve a 50- μ V peak-to-peak motor evoked potential (MEP) for at least five out of ten trials [56].

In each subject, the MT was titrated three times on three separate days. Each titration session included determination of two MTs corresponding to the two current polarities applied to the electrodes, which were then averaged to produce a single MT value per session. This average bidirectional MT is relevant to ECT since the ECT stimulus consists of current pulses with alternating polarity [17].

G. Neural Activation Threshold Estimation

Individual neural activation threshold was estimated from the median E-field strength in the FDI representation of motor cortex, E_{FDI} , at the stimulus pulse amplitude corresponding to the individual MT. Since there were three MT samples per subject, we obtained three neural threshold estimates per subject using the same individual model (since anatomy does not change) and the three different MTs (to capture physiological variability).

To sample the simulated E-field in the FDI regions, we created an anatomical template map that includes the FDI areas, which were manually delineated on the published macaque brain "F99" atlas [57] based on the rhesus macaque brain stereotaxic atlases [58], [59] and the web-based scalable brain atlas (<http://scalablebrainatlas.incf.org>). The primary motor cortical representation area of the hand at the precentral gyrus "hand knob" was determined from coronal MRI slices and verified in the axial plane [6], [60]. For segmentation of multiple NHP subjects, we developed an automatic algorithm for atlas-based region of interest segmentation using subroutines of SPM8. Each individual brain volume was warped to the atlas template in the least squares sense, thus minimizing the sum of squares difference between the subject and template image. This process computed a spatial transformation matrix that best registers the individual brain volume to the template [34]. Subsequently, the brain volume was aligned to the template map enclosing the FDI labels, and each voxel was labeled with the FDI structure label using the transformation matrix. Finally, the individual FDI

volume labels were created by transforming back into the native space through the inverse of the deformation field.

H. Correlation Between E-Field Model and MT

If the E-field models appropriately capture the individual anatomy that impacts MT, then the individual ratio between the simulated electrode current and induced E-field strength should be correlated with the measured MT. To evaluate this hypothesis, we calculated the ratio of the electrode current to the simulated median FDI E-field strength, $I_{\text{electrode}}/E_{\text{FDI}}$, for each subject, and correlated it with the measured MT using the Pearson's linear correlation coefficient. The $I_{\text{electrode}}/E_{\text{FDI}}$ ratio is expected to be correlated with the individual MTs since it characterizes the amount of current that has to be applied so that the FDI region in motor cortex reaches an approximately fixed neural activation threshold. The underlying assumption here is that the E-field threshold for neural activation, estimated by the median E_{FDI} value at the individually-titrated MT current, is comparable across subjects and would be expected to have less interindividual variability compared to the individual MTs. The extent to which this is the case will be evaluated as described in Section II-G.

I. Anatomical Correlates of E-Field Strength

To evaluate how macroscopic anatomical parameters affect the individual E-field models, we examined Pearson's linear correlation between $I_{\text{electrode}}/E_{\text{FDI}}$ and electrode-to-cortex distance under the two electrode centers, skin-to-cortex distance at vertex, and brain volume. This analysis is only exploratory since the sample was small and the various anatomical parameters considered are likely to be correlated with each other; therefore, we did not apply multiple comparison corrections or more sophisticated statistical analysis.

1) *Tissue Thickness*: Since the tissue thickness between the electrode and cortex is a critical determinant of the amount of stimulus current reaching the cortex, we examined the relations between the measured MT and the electrode-to-cortex distance under the electrode centers as well as the skin-to-cortex distance at vertex. Calculation of these distances was performed in three dimensions using the outer skin and cortical surface meshes. The distance from slice views in two dimensions would result in overestimation of the skin-to-cortex distance, since a closer distance could be found out-of-plane [61]. Therefore, for each node on the tessellated skin surface, we searched for the intersection along the direction of the surface normal at that node and the cortical surface. The skin-to-cortex thickness was then determined as the shortest distance between the two surfaces [62].

2) *Brain Region Volumes*: The volumes of gray matter, white matter, and extracerebral CSF excluding lateral ventricles were computed by multiplying the mean voxel value across the partial volume image by the total volume of that image [total volume = number of voxels \times voxel size ($0.5 \times 0.5 \times 0.5 \text{ mm}^3$)]. The total brain volume was determined by summation of each tissue volume fraction, finally divided by 1000 to obtain brain volume in milliliters (mL).

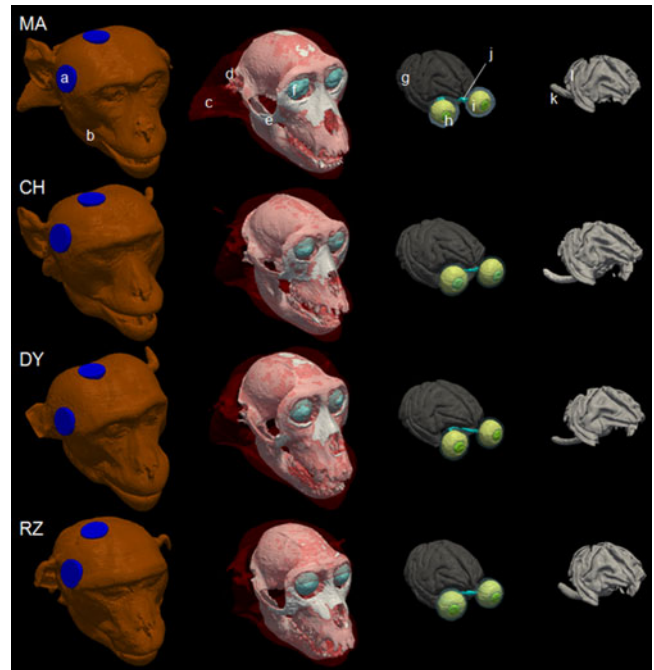


Fig. 2. Individual head models of the four NHP subjects (MA, CH, DY, and RZ, top to bottom rows, respectively) with RUL TES/ECT electrode configuration. The various conductivity compartments are labeled including (a) RUL stimulation electrodes and tissue segmentation masks including (b) skin, (c) muscle, (d) vertebrae, (e) skull compacta, (f) sclera, (g) gray matter, (h) lens, (i) eyeball, (j) optic nerve, (k) spinal cord, and (l) white matter.

III. RESULTS

A. Individual Head Models

The four individualized NHP head models (subjects MA, CH, DY, and RZ) used for the TES/ECT E-field simulation are displayed in Fig. 2. The segmented tissue regions included skin, muscle, vertebrae, skull compacta, skull spongiosa, CSF, sclera, gray matter, lens, eyeball, optic nerve, spinal cord, sinus, and white matter. The geodesic distance from electrode center to electrode center varied across subjects due to interindividual differences in anatomy, and was estimated to be 53.7, 46.7, 57.9, and 47.3 mm for MA, CH, DY, and RZ, respectively.

B. Interindividual Variation in Electric Field Strength

The interindividual variation in E-field strength due to anatomical differences between the subjects was investigated at fixed current amplitude of 800 mA (conventional current amplitude for ECT). Fig. 3 shows descriptive statistics [first, 25th, 50th (median), 75th, and 99th percentiles] of the simulated E-field strength in the whole brain for the four subjects. The 99th percentile of the simulated E-field strength was used as a robust measure of peak strength that limits the influence of outliers resulting from possible computational instabilities [63].

Subject RZ has the highest median E-field strength (1.59 V/cm) in the whole brain, whereas subject CH has the lowest E-field (1.01 V/cm), thus resulting in a 57% variation in median E-field value in the whole brain across the four subjects. The ratio of the median E-field values between the right

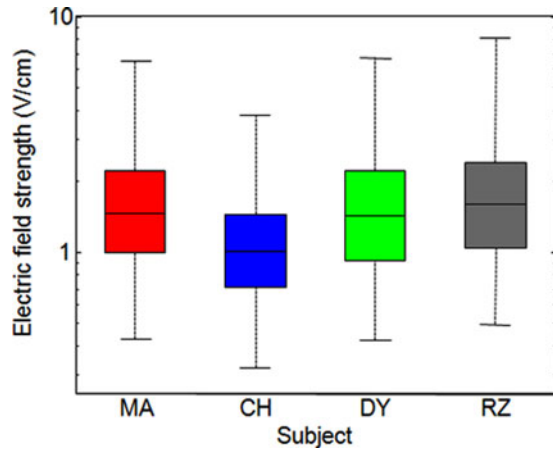


Fig. 3. Simulated E-field strength (magnitude) in the brain induced by the TES/ECT RUL electrode configuration at 800-mA current for the four NHP subjects. The E-field strength (y-axis) is shown on a logarithmic scale to normalize the skewed E-field distribution. Boxes indicate the interquartile range (25th to 75th percentile) with the median marked by the horizontal line within the box, and whiskers delimit the first and 99th percentiles of the distribution.

and left hemispheres was 1.72 ± 0.15 , which is expected since the RUL electrode configuration targets preferentially the right hemisphere. Finally, the coefficient of variation of the median E-field in the FDI region, E_{FDI} , across all subjects was 22%.

C. Interindividual Variation in MT

Fig. 4(a) shows the RUL TES MTs for each subject averaged across the three titration sessions. The average MT across the four NHP subjects is 80.33 mA, with a range of 50–120 mA (2.4-fold variation) and coefficient of variation of 37%. A one-way analysis of variance (ANOVA) showed a significant difference in MT across the subjects ($F(3, 8) = 18.65, p = 0.0006$). Post-hoc Tukey HSD test revealed that at the $p < 0.05$ significance level, the MT for subject CH was different from all other subjects and the MTs for subjects DY and MA differed from each other.

D. Electric Field Distribution at MT

Fig. 5 shows a set of representative views for the spatial E-field magnitude distribution at current strength corresponding to the individual MT for the four NHP subjects. The results in Fig. 5 demonstrate that, as expected, the lateralized RUL electrode configuration predominantly stimulates the superior regions of the right hemisphere, including the FDI representation in the right motor cortex. Nevertheless, the detailed E-field distribution is complicated due to the heterogeneous and anisotropic electrical conductivity structure of the head as well as interindividual variation in the head anatomy.

E. Estimated Neural Activation Threshold

The E-field threshold for neural activation was estimated from the simulated E-field strength in the FDI representation in motor cortex at the individual MT current (illustrated in Fig. 5). Fig. 4(b) shows the estimates of the E-field threshold for neural activation for each subject. The average neural activation

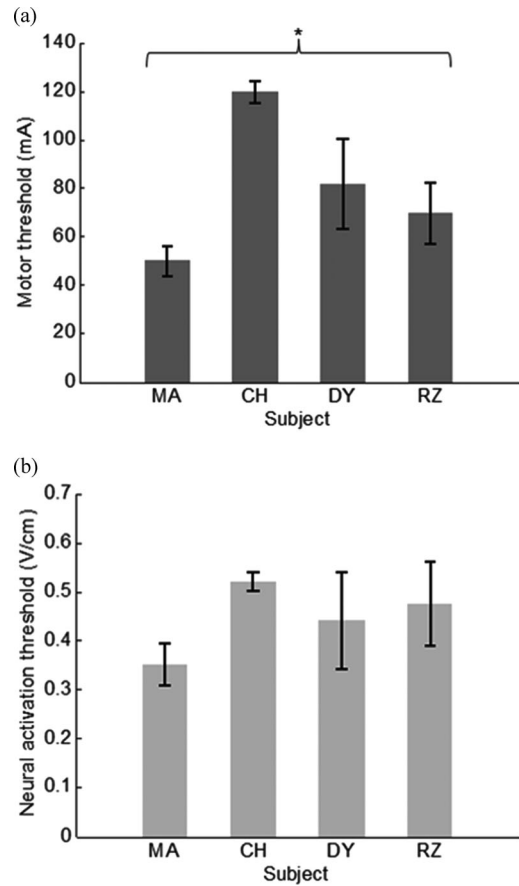


Fig. 4. (a) Measured individual amplitude-titrated RUL TES MT for 0.2-ms pulse width for the four NHP subjects. (*) The MT for subject CH was different from all other subjects and the MTs for subjects DY and MA differed from each other ($p < 0.05$). (b) Corresponding estimated E-field neural activation threshold in the motor cortex representation of FDI, computed from the data in (a) and the individual E-field models. The neural activation threshold estimates did not differ significantly among subjects. Bars show mean values and error bars show standard deviation associated with the three MT measurements for each subject.

threshold across the four NHP subjects is 0.45 V/cm (standard deviation = 0.07, coefficient of variation = 16%). Subjects CH and MA yielded the highest and lowest neural activation threshold estimates, 0.52 and 0.35 V/cm, respectively. In contrast to the differences in MT, we found no significant interindividual difference in the estimated neural activation thresholds ($F(3, 8) = 3.15, p = 0.087$).

F. E-Field Model Correspondence With MT

Fig. 6 shows the correlation between the measured MT and the $I_{\text{electrode}}/E_{FDI}$ ratio computed from the individual FEM simulation. The significant correlation ($r^2 = 0.95, p = 0.026$) suggests that the FEM model could predict the variation in the empirical MT.

G. E-Field Strength Dependence on Anatomical Parameters

Quantifying one aspect of the head anatomy, Fig. 7(a) shows individual maps of the distance from the skin surface to the

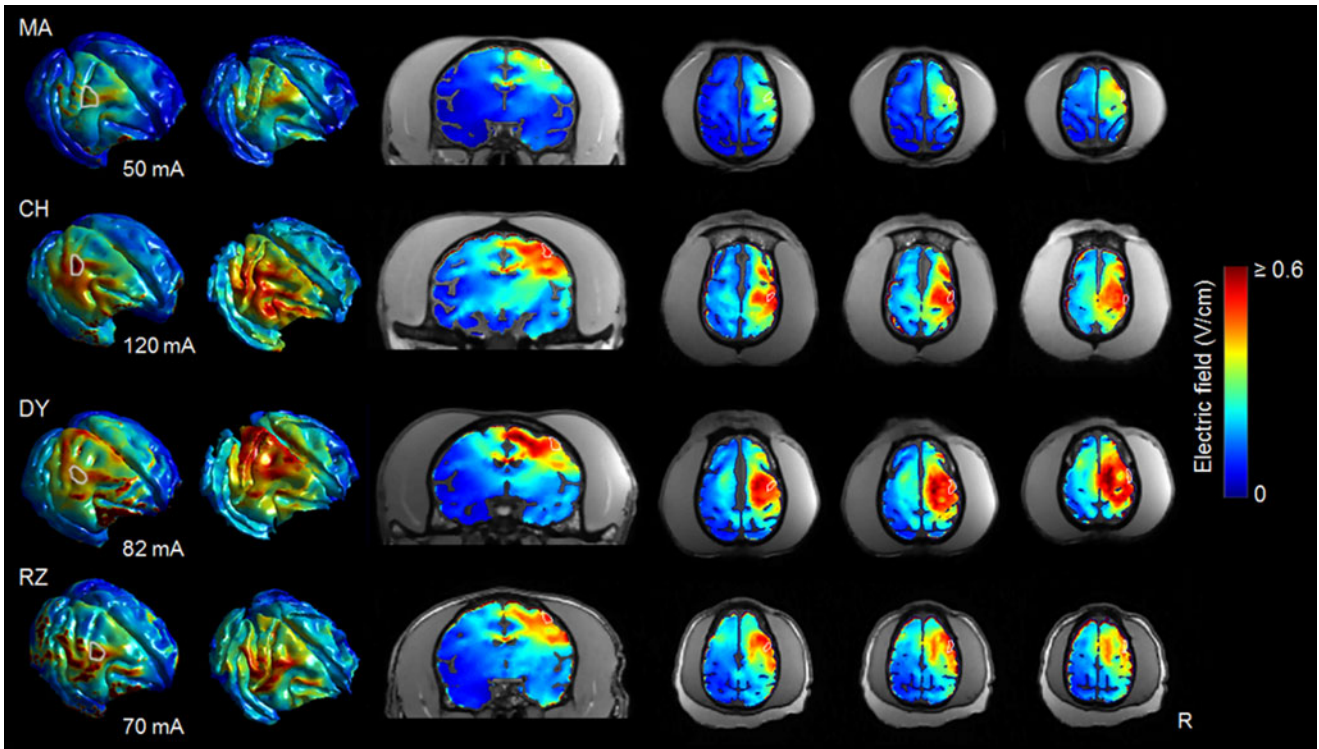


Fig. 5. Simulated E-field distribution at current strength corresponding to the measured individual MT for the four NHP subjects (MA, CH, DY, and RZ, top to bottom rows, respectively). Shown are E-field maps on the cortical surface (CSF–gray matter interface; first column), white matter surface (gray matter–white matter interface; second column), representative coronal slice (third column), and transaxial slices (fourth to six columns; 1.5-mm interslice distance). The structural MRI images of the extracerebral brain tissues are shown in gray around the slices as a reference for the anatomical results in Fig. 7. Region-of-interest outlines in white show the FDI representation in motor cortex. Individual average MT is shown on the left below each row. R: right.

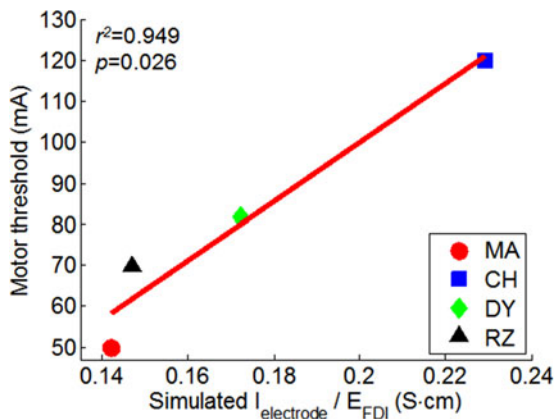


Fig. 6. Correlation between the average measured MT and the $I_{\text{electrode}}/E_{\text{FDI}}$ ratio computed from the individual FEM simulations of RUL TES/ECT. Pearson's correlation r^2 and p values are given in the correlation plot.

cortex surface in the four NHP subjects. Subjects RZ and DY had the lowest (16.4 ± 6.9 mm) and highest mean distance (18.8 ± 8.4 mm), respectively, corresponding to 15% interindividual variation. There are also differences in the skin-to-cortex distance at various points on the scalp—lateral areas have larger skin-to-cortex distance compared to the vicinity of the vertex.

Fig. 7(b)–(e) shows an exploratory analysis of the correlations between the simulated $I_{\text{electrode}}/E_{\text{FDI}}$ ratio and several anatom-

ical measures. The correlations between $I_{\text{electrode}}/E_{\text{FDI}}$ and the superior electrode-to-cortex distance, vertex-to-cortex distance, and brain volume are significant ($r^2 > 0.96$, $p < 0.02$). On the other hand, there was no significant correlation between $I_{\text{electrode}}/E_{\text{FDI}}$ and the electrode-to-cortex distance for the right frontotemporal electrode ($r^2 = 0.37$, $p = 0.39$), which is 2–4 times further from the cortex than the superior electrode.

IV. DISCUSSION

A. FE Modeling of NHP for TES/ECT

We presented a modeling pipeline for generating anatomically realistic FEM representations of the NHP head incorporating complex tissue geometries and white matter anisotropic conductivities, and used it to simulate the E-field generated by RUL TES/ECT. This platform can be also used for modeling of other forms of brain stimulation such as TMS, transcranial direct current stimulation, and focused ultrasound.

Our model creation platform consists of a combination of freely available software tools including 3-D Slicer, FSL, SPM, and ITK-SNAP, that are continually refined and supported. This platform is capable of generating the FEM model in a format importable into FEM software packages other than ANSYS, such as COMSOL, Abaqus, or SCIRun (freeware). Alternative approaches for modeling human brain stimulation paradigms have used open-source packages such as TetGen [64]–[66], SCIRun

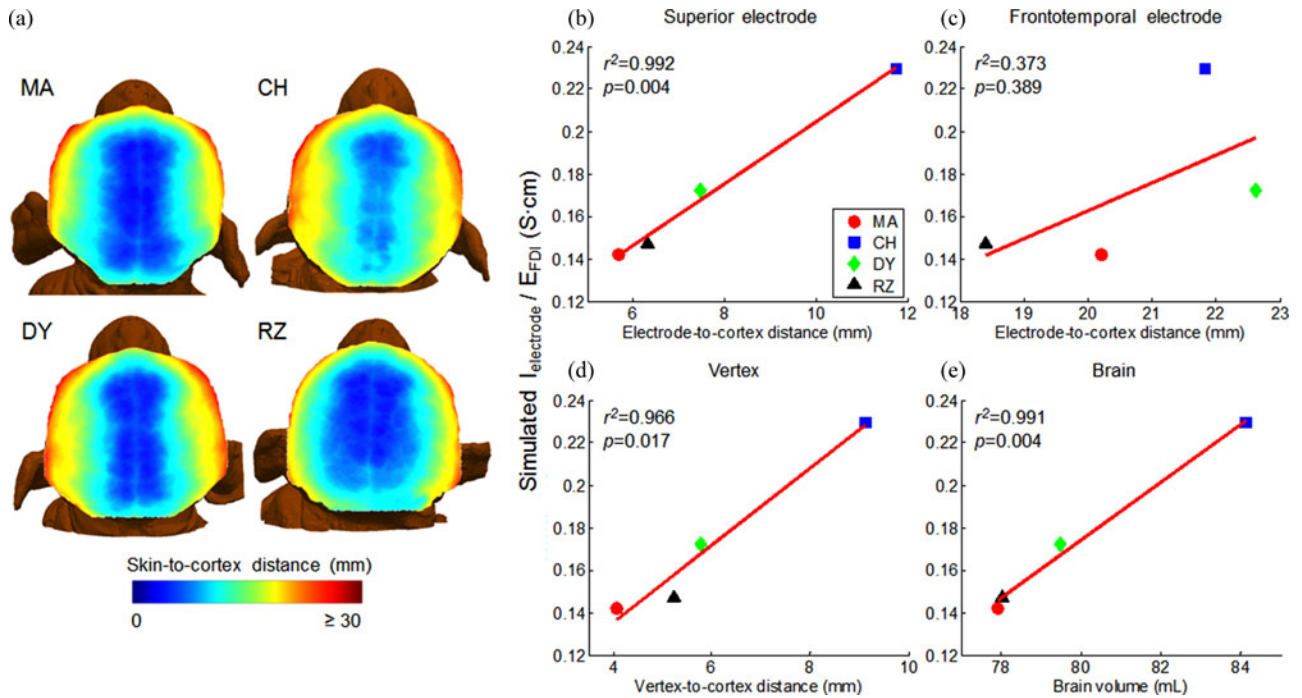


Fig. 7. (a) Maps of the distance from the skin surface to the cortex surface plotted over the head surface for the four NHP subjects, measured from the MRI data. Correlation between the simulated $I_{\text{electrode}}/E_{\text{FDI}}$ ratio and the measured (b), (c) electrode-to-cortex distance under superior or frontotemporal electrodes, (d) vertex-to-cortex distance, and (e) individual brain volume. Pearson's correlation r^2 and p values are given in each correlation plot.

[67], and GetFEM++ [68] or commercial software (e.g., ScanIP [12], [69]).

While the E-field simulations were not validated directly, the range of E-field magnitudes in Fig. 3 is consistent with intracerebral E-field recordings in two rhesus macaques that we reported previously [1], [70]. Specifically, the average median E-field in the brain in the present study is 1.38 V/cm with maximum values of over 8 V/cm with RUL electrodes at 800-mA stimulus current. Under the same stimulation conditions, we measured median E-field of 5.12 V/cm in central portions of the brain [70]. In the latter publication the two subjects were different, younger (age = 2–4 years), and lighter (weight = 3.1–5.4 kg) than the subjects in this study; therefore, the higher E-field in the brain is expected due to the smaller head size and thinner scalp of younger subjects.

At present, there are no published validations of high-resolution E-field models with direct measurements in the same subjects, although an ongoing effort in this direction has been announced [71]. Other approaches to validate the accuracy of the FEM forward models have been indirect, for example, by comparing to scalp potential [69] or neurophysiological measurements [12], [13]. Indeed, the significant correlation we found between the individual MT and the modeled $I_{\text{electrode}}/E_{\text{FDI}}$ ratio can be considered an indirect physiological validation of the ability of the models to capture the individual anatomy.

B. Interindividual Variation in Electric Field Strength due to Anatomical Variability

We showed that the E-field strength and spatial distribution varies due to anatomical differences among the four NHP sub-

jects. The results in Fig. 3 indicating 1.6-fold variation in E-field strength in the brain are consistent with published modeling studies in the context of transcranial direct current stimulation (tDCS) that reported 1.5-to-3-fold variation in peak cortical E-field or current density in normal human subjects [12], [72]. Our results support and extend these findings in the context of an ECT electrode configuration and NHP subjects. Due to this interindividual anatomical variation, applying fixed stimulus current amplitude to all ECT patients can result in different E-field exposure in the brain, yielding potentially variable clinical outcomes in terms of both therapeutic efficacy and adverse side effects. These observations support individualizing the ECT current amplitude as a means of compensating for interindividual variability in head anatomy to effect more focal stimulation with potentially fewer side effects [3], [16], [17]. For example, in this study, individualization of the stimulus current by the MT reduced the E-field variation in the target motor area by 27%.

C. E-Field Model Predicts Individual Variability in TES MT

We found that the ratio of the electrode current to the E-field strength in the FDI cortical area, $I_{\text{electrode}}/E_{\text{FDI}}$, calculated from the individualized E-field models is significantly correlated with MT. This correlation suggests that the subject-specific computational models predict variation in the individual current required for neural stimulation in ECT and in other forms of TES. These findings suggest that to compensate for individual anatomical variability, individual E-field simulation could be used to choose the TES/ECT current amplitude.

We also found that the $I_{\text{electrode}}/E_{\text{FDI}}$ ratio is significantly correlated with the individual brain volume as well as the

skin-to-cortex distance at vertex and under the superior electrode, suggesting that these macroscopic anatomical parameters explain some of the individual E-field strength variability. On the other hand, there was no significant correlation between the $I_{\text{electrode}}/E_{\text{FDI}}$ ratio and the skin-to-cortex distance under the right frontotemporal electrode. This could potentially be explained by the significantly larger distances from the lateral electrode to the underlying cortex as well as the FDI cortical area, due to the thick lateral muscles in the NHP, which cause more diffusion of the current injected by the electrode.

Finally, due to the limited sample size and the significant correlation between the modeled MT and some of the macroscopic anatomical parameters, we could not conduct analysis of which is a better predictor of the measured MT.

D. Neural Activation Threshold

Based on the individual MTs of the left FDI muscle and the individual realistic E-field models, the neural activation threshold was estimated to be 0.45 ± 0.07 V/cm for 0.2-ms rectangular pulses. The 16% variation in the estimated neural activation threshold across subjects is smaller than the variation in MT (37%), indicating that the individualized FEM models indeed account for interindividual differences in head anatomy as discussed in the previous section. For comparison, a study of TES in anesthetized humans yielded an E-field threshold range of 0.45–1.12 V/cm for 0.05-ms pulse width [73]. In addition, the E-field threshold from studies using TMS with a figure-eight coil ranges from 0.3 to 1.3 V/cm [74]–[77]. Previously, we used these data and information on the neural membrane time constant in motor cortex to estimate the neural activation threshold for various pulse widths [21], obtaining 0.29 V/cm for 0.2-ms pulse width. These prior threshold estimates are largely consistent with the estimate from this study, considering that both this and prior studies have various limitations, which are discussed below.

E. Limitations

This study has several potential limitations. First, the study involves a small number of subjects; therefore, the interindividual variability and correlation analyses should be interpreted with caution.

Second, there are possible source of errors related to the construction of the E-field models which are common to virtually all modeling studies of this kind. The accuracy of the E-field/current density fields induced in the head by TES is influenced by tissue electrical properties [15], [26], [55]. Since accurate *in vivo* measurement of the tissue conductivities is not feasible at present, the model accuracy depends on how well the tissue conductivity values from the literature match the actual conductivities, which is unknown. Nevertheless, conductivity errors would affect the absolute E-field values more so that the relative values across subjects, thus interindividual measures, which are the focus of this paper, would be less affected. The E-field sensitivity to variations in tissue layer thickness and conductivity has been examined in detail in our previous study [15]. The model accuracy is also affected by potential errors in the individual tissue

segmentation and modeled electrode placement [16]. By applying the same processing pipeline, including the same operator carrying out the manual segmentation adjustments, to the models for all subjects, we aimed to avoid differential errors across subjects.

Finally, the neural activation threshold estimate is subject to several assumptions. We assume that neural activation had the lowest threshold in the FDI representation in motor cortex. However, we cannot exclude that direct neural activation may have occurred along the corticospinal tract away from the cortical representation of FDI. Nevertheless, the significant correlation between the MT and the E-field in the cortical FDI control area, as shown in Fig. 6, provides some support for a cortical origin of the MEPs. Furthermore, for robustness we considered the median E-field value in the FDI motor cortex as representative of the threshold, but subregions with higher E-field within the FDI may have been the triggering points. Finally, in estimating the neural activation threshold we took into account only the E-field magnitude but not its direction, which may influence the neural activation threshold [21], [78]. Directionality of the activation threshold is difficult to predict as it potentially depends on the morphology and orientation relative to the E-field of various neural populations and neural elements, including cortical interneurons, pyramidal neurons, and fibers of passage. Determining these interactions is beyond the scope of this paper. Nevertheless, for future studies addressing directionality effects, the diffusion tensor data that are incorporated in our modeling pipeline could be used to estimate characteristics of the neural fibers.

V. CONCLUSION

We developed high-resolution individual-specific FEM models of NHP heads and used these models to simulate the E-field in the brain generated by the RUL ECT electrode configuration. The models provide insight into how individual anatomical differences among the NHPs affect the E-field distribution generated by TES/ECT, and allowed the estimation of the E-field threshold for neural activation. While the study included only four subjects, the significant correlation between the measured and modeled MT suggests that the models appropriately capture interindividual anatomical variability. Furthermore, our exploratory analysis indicated that the interindividual differences of the E-field strength in the brain are driven by macroscopic parameters of the head anatomy. This study can contribute insight in NHP studies of ECT and other brain stimulation interventions, help link the results to clinical studies, and ultimately lead to more rational brain stimulation dosing paradigms such as individualization of the ECT current amplitude.

ACKNOWLEDGMENT

The authors would like to thank C. Sikes-Keilp, M. Aly, B. Chan, N. Reyes, M. A. Rosa, and N. Youssef for assisting in the NHP procedures and data entry. W. H. Lee is inventor on invention disclosure to Duke University on the models presented in this paper. In the past two years, S. H. Lisanby has served as Principal Investigator on industry-sponsored research grants to

Duke (ANS/St. Jude Medical, NeoSync, Brainsway, Nexstim); equipment loans to Duke (Magstim, MagVenture); is coinventor on a patent and patent applications on TMS technology; and has no consultancies, speakers bureau memberships, board affiliations, or equity holdings in related device industries. A. F. Laine reports no relevant financial disclosures. A. V. Peterchev is inventor on patents, patent applications, and invention disclosures on TMS and ECT technology assigned to Columbia University and Duke University, from which he has received royalties. He has received research support from Rogue Research, Tal Medical, and MagVenture.

REFERENCES

- [1] S. H. Lisanby *et al.*, "Neurophysiological characterization of magnetic seizure therapy (MST) in non-human primates," *Suppl. Clin. Neurophysiol.*, vol. 56, pp. 81–99, 2003.
- [2] T. D. Moscrip *et al.*, "A primate model of anterograde and retrograde amnesia produced by convulsive treatment," *J. ECT*, vol. 20, no. 1, pp. 26–36, 2004.
- [3] A. V. Peterchev *et al.*, "Individualized low amplitude seizure therapy: Minimizing current for electroconvulsive therapy and magnetic seizure therapy," *Neuropsychopharmacology*, to be published.
- [4] A. V. Peterchev *et al.*, "Optimal frequency for seizure induction," *J. ECT*, vol. 26, pp. 154–154, 2010.
- [5] T. Spellman *et al.*, "Focal electrically administered seizure therapy: A novel form of ECT illustrates the roles of current directionality, polarity, and electrode configuration in seizure induction," *Neuropsychopharmacology*, vol. 34, no. 8, pp. 2002–2010, 2009.
- [6] F. Amaya *et al.*, "Transcranial magnetic stimulation and PAS-induced cortical neuroplasticity in the awake rhesus monkey," *Clin. Neurophysiol.*, vol. 121, no. 12, pp. 2143–2151, 2010.
- [7] F. S. Salinas *et al.*, "Functional neuroimaging of the baboon during concurrent image-guided transcranial magnetic stimulation," *Neuroimage*, vol. 57, no. 4, pp. 1393–1401, 2011.
- [8] A. Gerits *et al.*, "Transcranial magnetic stimulation of macaque frontal eye fields decreases saccadic reaction time," *Exp. Brain Res.*, vol. 212, no. 1, pp. 143–152, 2011.
- [9] A. Valero-Cabre *et al.*, "Frontal non-invasive neurostimulation modulates antisaccade preparation in non-human primates," *PLoS One*, vol. 7, no. 6, art. no. e38674, 2012.
- [10] J. K. Mueller *et al.*, "Simultaneous transcranial magnetic stimulation and single-neuron recording in alert non-human primates," *Nat. Neurosci.*, vol. 17, no. 8, pp. 1130–1136, 2014.
- [11] T. Deffieux *et al.*, "Low-intensity focused ultrasound modulates monkey visuomotor behavior," *Current Biol.*, vol. 23, no. 23, pp. 2430–2433, 2013.
- [12] D. Edwards *et al.*, "Physiological and modeling evidence for focal transcranial electrical brain stimulation in humans: A basis for high-definition tDCS," *Neuroimage*, vol. 74, pp. 266–275, 2013.
- [13] A. Opitz *et al.*, "Physiological observations validate finite element models for estimating subject-specific electric field distributions induced by transcranial magnetic stimulation of the human motor cortex," *Neuroimage*, vol. 81C, pp. 253–264, 2013.
- [14] C. K. Loo *et al.*, "Revisiting frontoparietal montage in electroconvulsive therapy: Clinical observations and computer modeling: A future treatment option for unilateral electroconvulsive therapy," *J. ECT*, vol. 31, pp. e.7–e.13, 2014.
- [15] Z. D. Deng *et al.*, "Effect of anatomical variability on electric field characteristics of electroconvulsive therapy and magnetic seizure therapy: A parametric modeling study," *IEEE Trans. Neural Syst. Rehabil. Eng.*, vol. 23, no. 1, pp. 22–31, 2015.
- [16] Z. D. Deng *et al.*, "Controlling stimulation strength and focality in electroconvulsive therapy via current amplitude and electrode size and spacing: Comparison with magnetic seizure therapy," *J. ECT*, vol. 29, no. 4, pp. 325–335, 2013.
- [17] A. V. Peterchev *et al.*, "Electroconvulsive therapy stimulus parameters: Rethinking dosage," *J. ECT*, vol. 26, no. 3, pp. 159–174, 2010.
- [18] S. Rossi *et al.*, "Safety, ethical considerations, and application guidelines for the use of transcranial magnetic stimulation in clinical practice and research," *Clin. Neurophysiol.*, vol. 120, no. 12, pp. 2008–2039, 2009.
- [19] J. C. Rothwell *et al.*, "Magnetic stimulation: Motor evoked potentials. The international federation of clinical neurophysiology," *Electroencephalogr. Clin. Neurophysiol. Suppl.*, vol. 52, pp. 97–103, 1999.
- [20] P. Julkunen *et al.*, "Within-subject effect of coil-to-cortex distance on cortical electric field threshold and motor evoked potentials in transcranial magnetic stimulation," *J. Neurosci. Methods*, vol. 206, no. 2, pp. 158–164, 2012.
- [21] Z. D. Deng *et al.*, "Electric field strength and focality in electroconvulsive therapy and magnetic seizure therapy: A finite element simulation study," *J. Neural Eng.*, vol. 8, no. 1, art. no. 016007, 2011.
- [22] W. H. Lee *et al.*, "Anatomical variability predicts individual differences in transcranial electric stimulation motor threshold," in *Proc. IEEE Conf. Eng. Med. Biol. Soc.*, 2013, pp. 815–818.
- [23] T. G. Reese *et al.*, "Reduction of eddy-current-induced distortion in diffusion MRI using a twice-refocused spin echo," *Magn. Reson. Med.*, vol. 49, no. 1, pp. 177–182, 2003.
- [24] T. Jaermann *et al.*, "Influence of SENSE on image properties in high-resolution single-shot echo-planar DTI," *Magn. Reson. Med.*, vol. 55, no. 2, pp. 335–342, 2006.
- [25] X. Liu *et al.*, "Optimization of in vivo high-resolution DTI of non-human primates on a 3 T human scanner," *Methods*, vol. 50, no. 3, pp. 205–213, 2010.
- [26] W. H. Lee *et al.*, "Regional electric field induced by electroconvulsive therapy in a realistic finite element head model: Influence of white matter anisotropic conductivity," *Neuroimage*, vol. 59, no. 3, pp. 2110–2123, 2012.
- [27] A. Fedorov *et al.*, "3D slicer as an image computing platform for the quantitative imaging network," *Magn. Reson. Imaging*, vol. 30, no. 9, pp. 1323–1341, 2012.
- [28] N. J. Tustison *et al.*, "N4ITK: Improved N3 bias correction," *IEEE Trans. Med. Imaging*, vol. 29, no. 6, pp. 1310–1320, 2010.
- [29] W. H. Lee *et al.*, "Methods and evaluations of MRI content-adaptive finite element mesh generation for bioelectromagnetic problems," *Phys. Med. Biol.*, vol. 51, no. 23, pp. 6173–6186, 2006.
- [30] J. Weickert, "A review of nonlinear diffusion filtering," *Scale-Space Theory Comput. Vis.*, vol. 1252, pp. 3–28, 1997.
- [31] M. J. Black *et al.*, "Robust anisotropic diffusion," *IEEE Trans. Image Process.*, vol. 7, no. 3, pp. 421–432, 1998.
- [32] S. M. Smith *et al.*, "Advances in functional and structural MR image analysis and implementation as FSL," *Neuroimage*, vol. 23, pp. S208–S219, 2004.
- [33] P. A. Yushkevich *et al.*, "User-guided 3D active contour segmentation of anatomical structures: Significantly improved efficiency and reliability," *Neuroimage*, vol. 31, no. 3, pp. 1116–1128, 2006.
- [34] J. Ashburner and K. J. Friston, "Unified segmentation," *Neuroimage*, vol. 26, no. 3, pp. 839–851, 2005.
- [35] Y. Huang *et al.*, "Automated MRI segmentation for individualized modeling of current flow in the human head," *J. Neural Eng.*, vol. 10, no. 6, art. no. 066004, 2013.
- [36] D. G. McLaren *et al.*, "A population-average MRI-based atlas collection of the rhesus macaque," *Neuroimage*, vol. 45, no. 1, pp. 52–59, 2009.
- [37] D. G. McLaren *et al.*, "Rhesus macaque brain morphometry: A methodological comparison of voxel-wise approaches," *Methods*, vol. 50, no. 3, pp. 157–165, 2010.
- [38] American Psychiatric Association, *The Practice of Electroconvulsive Therapy: Recommendations for Treatment and Privileging: A Task Force Report of the American Psychiatric Association*. Washington, DC, USA: American Psychiatric Pub, 2001.
- [39] C. A. Bossetti *et al.*, "Analysis of the quasi-static approximation for calculating potentials generated by neural stimulation," *J. Neural Eng.*, vol. 5, no. 1, pp. 44–53, 2008.
- [40] J. P. Pons *et al.*, "High-quality consistent meshing of multi-label datasets," *Inf. Process. Med. Imaging*, vol. 20, pp. 198–210, 2007.
- [41] K. A. Awada *et al.*, "Effect of conductivity uncertainties and modeling errors on EEG source localization using a 2-D model," *IEEE Trans. Biomed. Eng.*, vol. 45, no. 9, pp. 1135–1145, 1998.
- [42] C. H. Wolters *et al.*, "Influence of tissue conductivity anisotropy on EEG/MEG field and return current computation in a realistic head model: A simulation and visualization study using high-resolution finite element modeling," *Neuroimage*, vol. 30, no. 3, pp. 813–826, 2006.
- [43] R. J. Sadleir *et al.*, "Transcranial direct current stimulation (tDCS) in a realistic head model," *Neuroimage*, vol. 51, no. 4, pp. 1310–1318, 2010.
- [44] G. Gabriel *et al.*, "The dielectric properties of biological tissues: I. Literature survey," *Phys. Med. Biol.*, vol. 41, no. 11, pp. 2231–2249, 1996.

- [45] R. N. Holdefer *et al.*, "Predicted current densities in the brain during transcranial electrical stimulation," *Clin. Neurophysiol.*, vol. 117, no. 6, pp. 1388–1397, 2006.
- [46] S. B. Baumann *et al.*, "The electrical conductivity of human cerebrospinal fluid at body temperature," *IEEE Trans. Biomed. Eng.*, vol. 44, no. 3, pp. 220–223, 1997.
- [47] P. J. Basser *et al.*, "Estimation of the effective self-diffusion tensor from the NMR spin-echo," *J. Magn. Reson. Series B*, vol. 103, no. 3, pp. 247–254, 1994.
- [48] D. C. Alexander *et al.*, "Spatial transformations of diffusion tensor magnetic resonance images," *IEEE Trans. Med. Imaging*, vol. 20, no. 11, pp. 1131–1139, 2001.
- [49] D. Gullmar *et al.*, "Influence of anisotropic electrical conductivity in white matter tissue on the EEG/MEG forward and inverse solution. A high-resolution whole head simulation study," *Neuroimage*, vol. 51, no. 1, pp. 145–163, 2010.
- [50] H. Hallez *et al.*, "Dipole estimation errors due to not incorporating anisotropic conductivities in realistic head models for EEG source analysis," *Phys. Med. Biol.*, vol. 54, no. 20, pp. 6079–6093, 2009.
- [51] H. Hallez *et al.*, "Dipole estimation errors due to differences in modeling anisotropic conductivities in realistic head models for EEG source analysis," *Phys. Med. Biol.*, vol. 53, no. 7, pp. 1877–1894, 2008.
- [52] H. S. Suh *et al.*, "Influence of anisotropic conductivity in the skull and white matter on transcranial direct current stimulation via an anatomically realistic finite element head model," *Phys. Med. Biol.*, vol. 57, no. 21, pp. 6961–6980, 2012.
- [53] W. H. Lee and T. S. Kim, "Methods for high-resolution anisotropic finite element modeling of the human head: Automatic MR white matter anisotropy-adaptive mesh generation," *Med. Eng. Phys.*, vol. 34, no. 1, pp. 85–98, 2012.
- [54] W. H. Lee *et al.*, "Influence of white matter anisotropic conductivity on EEG source localization: Comparison to fMRI in human primary visual cortex," *Clin. Neurophysiol.*, vol. 120, no. 12, pp. 2071–2081, 2009.
- [55] G. Ruffini *et al.*, "Transcranial current brain stimulation (tCS): Models and technologies," *IEEE Trans. Neural Syst. Rehabil. Eng.*, vol. 21, no. 3, pp. 333–345, 2013.
- [56] P. M. Rossini *et al.*, "Non-invasive electrical and magnetic stimulation of the brain, spinal cord and roots: Basic principles and procedures for routine clinical application. Report of an IFCN committee," *Electroencephalogr. Clin. Neurophysiol.*, vol. 91, no. 2, pp. 79–92, 1994.
- [57] D. C. Van Essen, "Surface-based atlases of cerebellar cortex in the human, macaque, and mouse," *Ann. N. Y. Acad. Sci.*, vol. 978, pp. 468–479, 2002.
- [58] G. Paxinos *et al.*, *The Rhesus Monkey Brain in Stereotaxic Coordinates*. San Diego, CA, USA: Academic, 2000.
- [59] K. S. Saleem and N. K. Logothetis, *A Combined MRI and Histology Atlas of the Rhesus Monkey Brain in Stereotaxic Coordinates*. Amsterdam, The Netherlands: Elsevier, 2007.
- [60] T. A. Yousry *et al.*, "Localization of the motor hand area to a knob on the precentral gyrus. A new landmark," *Brain*, vol. 120, no. (Pt 1), pp. 141–157, 1997.
- [61] M. S. Beauchamp *et al.*, "The developmental trajectory of brain-scalp distance from birth through childhood: Implications for functional neuroimaging," *PLoS One*, vol. 6, no. 9, art. no. e24981, 2011.
- [62] B. Fischl and A. M. Dale, "Measuring the thickness of the human cerebral cortex from magnetic resonance images," *Proc. Natl. Acad. Sci. USA*, vol. 97, no. 20, pp. 11050–11055, 2000.
- [63] M. Parazzini *et al.*, "Transcranial direct current stimulation: Estimation of the electric field and of the current density in an anatomical human head model," *IEEE Trans. Biomed. Eng.*, vol. 58, no. 6, pp. 1773–1780, 2011.
- [64] S. M. Rampersad *et al.*, "Simulating transcranial direct current stimulation with a detailed anisotropic human head model," *IEEE Trans. Neural Syst. Rehabil. Eng.*, vol. 22, no. 3, pp. 441–452, 2014.
- [65] H. Si, "Adaptive tetrahedral mesh generation by constrained Delaunay refinement," *Int. J. Numer. Methods Eng.*, vol. 75, no. 7, pp. 856–880, 2008.
- [66] C. H. Im *et al.*, "Evaluation of local electric fields generated by transcranial direct current stimulation with an extracephalic reference electrode based on realistic 3D body modeling," *Phys. Med. Biol.*, vol. 57, no. 8, pp. 2137–2150, 2012.
- [67] M. Dannhauer *et al.*, "A pipeline for the simulation of transcranial direct current stimulation for realistic human head models using SCIRun/BioMesh3D," in *Proc. IEEE Conf. Eng. Med. Biol. Soc.*, 2012, pp. 5486–5489.
- [68] M. Windhoff *et al.*, "Electric field calculations in brain stimulation based on finite elements: An optimized processing pipeline for the generation and usage of accurate individual head models," *Human Brain Mapping*, vol. 34, no. 4, pp. 923–935, 2013.
- [69] A. Datta *et al.*, "Validation of finite element model of transcranial electrical stimulation using scalp potentials: Implications for clinical dose," *J. Neural Eng.*, vol. 10, no. 3, art. no. 036018, 2013.
- [70] A. V. Peterchev *et al.*, "Measurement of intracerebral electric field induced by electroconvulsive therapy," *J. ECT*, vol. 28, no. 2, pp. 146–147, 2012.
- [71] B. Lafon *et al.*, "Direct experimental validation of computational current flow models with intra-cranial recordings in human and non-human primates," in *Proc. NYC Neuromodulation Conf. (2015)*. [Online]. Available: neuromodec.com/events/nyc-neuromodulation-conference-2015/abstracts/
- [72] A. Datta, D. Truong, P. Minhas, L. C. Parra, and M. Bikson, "Inter-individual variation during transcranial direct current stimulation and normalization of dose using MRI-derived computational models," *Frontiers Psychiatry*, vol. 3, no. 91, 2012, doi: 10.3389/fpsy.2012.00091.
- [73] B. Calancie *et al.*, "“Threshold-level” multipulse transcranial electrical stimulation of motor cortex for intraoperative monitoring of spinal motor tracts: Description of method and comparison to somatosensory evoked potential monitoring," *J. Neurosurgery*, vol. 88, no. 3, pp. 457–470, 1998.
- [74] S. Komssi *et al.*, "Excitation threshold of the motor cortex estimated with transcranial magnetic stimulation electroencephalography," *Neuroreport*, vol. 18, no. 1, pp. 13–16, 2007.
- [75] A. Thielscher and T. Kammer, "Linking physics with physiology in TMS: A sphere field model to determine the cortical stimulation site in TMS," *Neuroimage*, vol. 17, no. 3, pp. 1117–1130, 2002.
- [76] C. M. Epstein *et al.*, "Localizing the site of magnetic brain stimulation in humans," *Neurology*, vol. 40, no. 4, pp. 666–670, 1990.
- [77] D. Rudiak and E. Marg, "Finding the depth of magnetic brain stimulation: A re-evaluation," *Electroencephalogr. Clin. Neurophysiol.*, vol. 93, no. 5, pp. 358–371, 1994.
- [78] T. Radman *et al.*, "Role of cortical cell type and morphology in subthreshold and suprathreshold uniform electric field stimulation *in vitro*," *Brain Stimulation*, vol. 2, no. 4, pp. 215–228, 2009.

Authors' photographs and biographies not available at the time of publication.